Southwest Research Institute (SwRI) Project 18.03562 "Evaluation of Tungsten Alloy Rods" Final Report

Subcontractor Report
prepared by

Kathryn Dannemann and James Walker

May 2000

IAT.R 0301

Institute for Advanced Technology
The University of Texas at Austin

IAT

20030616 118

REPORT DOCUMENTATION PAGE

Form Approved
OMB NO. 0704-0188

1. AGENCY USE ONLY (Leave blank)	2. REPORT DATE	3. REPORT TYPE AND DATES COVERED
	May 2000	Technical Report

4. TITLE AND SUBTITLE
Southwest Research Institute (SwRI) Project 18.03562
"Evaluation of Tungsten Alloy Rods"
Final Report

5. FUNDING NUMBERS
Contract # DAAD17-01-D-0001

6. AUTHOR(S)
Kathryn Dannemann and James Walker

7. PERFORMING ORGANIZATION NAME(S) AND ADDRESS(ES)
Institute for Advanced Technology
The University of Texas at Austin
3925 W. Braker Lane, Suite 400
Austin, TX 78759-5316

8. PERFORMING ORGANIZATION REPORT NUMBER
IAT.R 0301

9. SPONSORING / MONITORING AGENCY NAME(S) AND ADDRESS(ES)
U.S. Army Research Laboratory
ATTN: AMSRL-WM-B
Aberdeen Proving Ground, MD 21005-5066

10. SPONSORING / MONITORING AGENCY REPORT NUMBER

11. SUPPLEMENTARY NOTES
The views, opinions, and/or findings contained in this report are those of the author(s) and should not be considered as an official Department of the Army position, policy, or decision, unless so designated by other documentation.

12a. DISTRIBUTION / AVAILABILITY STATEMENT
Approved for public release; distribution unlimited.

12b. DISTRIBUTION CODE
A

13. ABSTRACT *(Maximum 200 words)*

This report summarizes the results of metallurgical evaluations conducted to assess the failure mechanism for tungsten alloy rods following dynamic fracture tests. Optical and electron microscopy evaluations were conducted on the six samples supplied. Based on these results, recommendations are provided for modeling the fracture process and for future fracture tests.

14. SUBJECT TERMS
tungsten alloy rods, dynamic fracture tests

15. NUMBER OF PAGES
34

16. PRICE CODE

17. SECURITY CLASSIFICATION OF REPORT	18. SECURITY CLASSIFICATION OF THIS PAGE	19. SECURITY CLASSIFICATION OF ABSTRACT	20. LIMITATION OF ABSTRACT
Unclassified	Unclassified	Unclassified	UL

TABLE OF CONTENTS

EVALUATION OF
TUNGSTEN ALLOY RODS

BACKGROUND

The Institute for Advanced Technology (IAT) requested the assistance of SwRI in investigating the failure process of several tungsten heavy alloy (WHA) rods following testing at high loading rates. Determination of the failure mechanism was desired for use in development of a fracture model for WHA penetrators. Six samples were supplied by IAT for evaluation following dynamic testing. The samples varied in composition and size depending on the type of test performed, and are identified in the following table. The transverse impact sample was a W-Ni-Fe alloy, while the other samples were W-Ni-Co alloys.

Sample ID	Test Type	No. of Pieces	Approximate Original Sample Dimensions (mm)	Alloy
Shot No. 74	Transverse Impact	2	4mm dia, 110mm long	91%W-7%Ni-3%Fe
Test A	Dynamic Bend	2	4 cm x 6mm x 6mm	91%W-6%Ni-3%Co (TeledyneX27X)
Test B	Dynamic Bend	2	4 cm x 6mm x 6mm	91%W-6%Ni-3%Co (TeledyneX27X)
Shot No. 225	Reverse Ballistic	5	2 mm dia, ~60 mm long	91%W-6%Ni-3%Co
Shot No. 226	Reverse Ballistic	2	2 mm dia, ~60 mm long	91%W-6%Ni-3%Co
Shot No. 227	Reverse Ballistic	3	2 mm dia, ~60 mm long	91%W-6%Ni-3%Co

TECHNICAL APPROACH

The objective of the metallurgical evaluation was to confirm the failure mechanism for the WHA samples following dynamic testing. To accomplish this objective, comparative analyses were performed on the six fractured samples supplied by IAT. It was assumed that these samples are representative of the three different test conditions. The following tasks were performed.

1. Stereomicroscopy

   The as-received samples were examined with a stereomicroscope for surface condition, dimensional assessment, etc. The as-received condition of the rods was documented photographically.

2. Fractography

Scanning electron microscopy was performed to establish the topographical features of the fracture surfaces for each sample supplied. These features were correlated with the mechanism of failure. Several fracture remnants were supplied for each of the rod penetrators from the reverse ballistic tests. Although stereomicroscopy was performed on each of the remnants supplied, only 1 or 2 pieces of the reverse ballistic test samples were evaluated by fractography and metallography. The reverse ballistic samples were chosen for these evaluations based on the stereomicroscopy evaluations.

3. Metallurgical Evaluation

The metallurgical microstructures of the six failed rods were compared by optical microscopy of mounted cross sections. This evaluation was a destructive analysis, and involved sectioning the tested samples. Sample preparation included cutting, mounting and polishing of the metallographic sections through the fracture. The sections of interest were mounted to allow microstructural evaluation normal to the fracture plane. For the rod penetrators tested in the reverse ballistic test, one remnant sample from each shot was mounted and evaluated for regions containing significant surface damage.

OBSERVATIONS

Dynamic Bend Tests

The material for the dynamic bend test samples was 91% W - 6% Ni – 3% Co (Teledyne X27X). According to the test details provided in Reference [1], a 600 kg weight was dropped 0.1 m onto the center of each sample while clamped on both ends. The samples had an original beam span of 4 cm and a 6 mm X 6 mm cross section. The impact velocity of the weight was calculated at approximately 1.4 m/s. This velocity is two orders of magnitude less than the impact velocity in the transverse impact test (i.e., 148 m/s). The plastic strain rates reported for the samples provided were 46.7 and 49.8 s^{-1}. Thus, the dynamic bend test samples experienced the lowest strain rate of the samples evaluated in this study.

The cross sections of the fractured bend samples were trapezoidal, as shown in Figure 1 for sample A. Both tensile and compressive fracture modes were operative, though the samples ultimately failed in tension. The compression component is due to bending. Several tensile cracks were detected in the mounted cross-sections on the opposite side of the sample from the bend (i.e., tensile side). The cracks were most prevalent in the vicinity of the fracture surface, as shown in Figure 2a. The longest tensile cracks measured approximately 0.15 to 0.17 mm long.

The cracks initiated at the tensile surface and progressed towards the compressive side of the sample in a direction approximately parallel to the fracture surface. Ultimate failure of the sample occurred in tension when the load capacity of the sample was exceeded due to competitive, crack growth processes from opposite sides of the sample diameter.

Higher magnification microscopy of the mounted cross-sections revealed the tensile cracks progressed through some of the W particles, resulting in cleavage of the particles. Fracture of the W particles is evident in representative photos of the tensile cracks, illustrated in Figure 2. The cracks also progressed along W particle/matrix interfaces. Some W particle fractures were observed on the compressive side of the samples near the initial bend region. A limited number of isolated W particle fractures and W particle/matrix fractures were detected towards the center of the sample cross section. Some fractured W particles were observed along the fracture surface on both the tensile and compressive sides of the samples evaluated. Particle fractures were more prevalent on the tensile fracture surface. Some W particle-particle decohesion was detected for W particles just beneath the fracture surface. Depending on the microstructure, damage progressed from the debonded regions along adjacent particles or particle/matrix interfaces.

The W particles were somewhat elongated on the tensile side of the samples relative to the compressive side, central fracture region, and regions away from the fracture. The difference in aspect ratio of the W particles is evident upon comparison of Figures 2 and 3. Strains up to 150 % were calculated for the dynamic bend samples based on the extent of elongation of the tungsten particles on the tensile vs. compressive sides of the samples. Particle fracture likely initiated in the most highly strained particles.

SEM evaluation of the fracture surface confirmed the optical results. Cleavage fracture of the W particles occurred on the tensile side of the fracture, as shown in Fig. 4a. The fracture mode was more ductile towards the central region of the sample. The central region consists of failed intergranular matrix zones, composed of W facets and ductile dimples in the matrix regions. Some cleaved W particles were also detected, along with decohesion between adjacent W particles, and between the W particles and the matrix. Fig. 4b is representative of the central region of the fracture for Sample B. More matrix dimples and W facets were evident in the bend region on the compressive side of the fracture surface. However, W particle cleavage was still observed in the compressive region of the fracture. Compare the compressive region, shown in Fig. 4c, with the other locations on the fracture. Some precipitates are evident in the dimpled matrix regions (Fig. 4d).

Dynamic Transverse Impact

This test technique was developed at The University of Texas at Austin [2] to measure the resistance of rods to dynamic fracture under transverse loading. The WHA rod material was 91% W- 7% Ni- 3% Fe alloy, and differed from the W-Ni-Co material for the other samples evaluated. The rod was impacted with an aluminum (6063-O Al) impactor weighing 6.62 grams. The impact velocity was 148 m/s for the sample supplied, Shot 74. Although the strain rate was not indicated for this test sample, it likely exceeds that of the dynamic bend test samples based on the two order of magnitude difference in impact velocity. The WHA rod fractured in two pieces in the vicinity of the impact, as shown in Figure 5. The mass and length of the fractured pieces were 21.23 g and 21.43 g, and 54.221 mm and 53.888 mm.

Fractographic and metallographic evaluation of the fractured sample revealed the operation of competitive tensile and compressive fracture modes. The micrograph in Fig. 5b illustrates distinct tensile and compressive regions on the fracture surface. The Al impactor imparted a compressive load. Tensile loading occurred on the surface opposite the impact. Comparison of the microstructures in the tensile and compressive regions of the mounted cross section showed that elongation of the W particles was not as significant for this sample relative to the dynamic bend samples. Maximum strain levels approaching 20 to 40 % were calculated based on particle elongations.

Although a few fractured W particles were observed in the vicinity of the impact region, generally, W particle cleavage was not observed. The W particles remained intact along the fracture surface path as illustrated in Fig. 6. Note the intergranular nature of the fracture path. A limited number of cleaved W particles were evident at the transition region between the tensile and compressive fracture regions. Some W particle fractures were observed on the tensile surface. Although the number of particle fractures observed on the tensile surface was greater for this sample relative to the dynamic bend samples, the fractures only extended through the top two particle surface layers. These had not progressed to form tensile cracks as shown for the dynamic bend test samples in Fig. 2a.

Some W particle-particle and W particle-matrix decohesion were observed immediately beneath the fracture on the tensile side of the sample, and along the tensile surface (i.e. side opposite the impact location) in the vicinity of the fracture. Particle-particle decohesion in the vicinity of the fracture surface is highlighted in the micrographs in Figure 6. Minimal decohesion between contiguous W particles or at the particle-matrix interface was also observed in other regions throughout the sample. However, this occurred to a very limited extent and only at isolated locations. Dynamic fracture appeared to occur almost solely along W particle-particle and W particle-matrix interfaces in agreement with the earlier observations by Lankford, et al. [3-5]. Linkage of these debonded regions resulted in failure when the extent of decohesion had exceeded the load capacity of the sample.

Precipitates were visible in the microstructure of this test sample. These varied in size with some approaching the size of the W grains. The larger particles appeared as unsintered particles. Energy dispersive spectroscopy (EDS) revealed the particles were rich in aluminum and oxygen. Thus, the particles are likely due to process defects. The presence of these particles did not appear to affect dynamic fracture since the particles were not prevalent in the vicinity of the fracture surface.

The fractographic features detected in SEM evaluations of Shot 74 support the optical microscopy results. The features are similar to those reported previously by Lankford, et al. [3-5] for WHA materials following dynamic fracture at strain rates up to 1000 s^{-1}. Intergranular fracture is apparent in the SEM micrographs in Fig. 7. The photos show representative areas from the tensile, compressive and central regions of the fracture and confirm that dynamic fracture occurred along tungsten particle and tungsten-matrix interfaces. Macroscopic dimples surrounding individual W grain facets were evident in each of the three regions. Some W particle cleavage was evident for the compressive region (Fig. 7d) near the impact location. Except for some pores surrounding the W facets (see Fig. 7b), there is little evidence of any plastic flow. Dimples in the matrix regions are not as apparent in the W-Ni-Fe dynamic transverse impact sample relative to the W-Ni-Co dynamic bend samples discussed in the previous section. Note the differences in matrix plastic flow upon comparison of Figs. 4 and 7 for the dynamic bend and dynamic transverse fracture test samples. This difference can be attributed to material differences and strain rate differences.

Reverse Ballistic Tests

These tests were conducted using a steel target and a 2 mm diameter WHA rod penetrator. The approximate strain rate was highest for the reverse ballistic test samples, and was approximately 10^4 to 10^5 s^{-1} in the vicinity of the plastically-flowing penetrating end of the projectile. The tungsten alloy utilized for the reverse ballistic test samples was the same as for the dynamic bend samples: 91% W-6% Ni – 3% Co (Teledyne X27X).

The as-received condition of the remnants from each shot (Shot 225, 226 and 227) is shown in Fig. 8. Impact damage from the target occurred along the surface where the yawed target impacted the W rod. Mushrooming of the impact surface was observed for Shots 226 (Remnant 2, Fig. 8b) and 227 (Remnant 3, Fig. 8c). The extent of mushrooming and surface impact damage is shown in the enlarged view of Shot 227, Fig. 9. The mushrooming phenomenon is characteristic of penetration and is further described for WHA in Ref. [6]. Shear localization occurs after the development of the mushroomed head (i.e., shear localization occurs at a high strain).

Optical microscopy of one sample each for Shots 225 (remnant 3), 226 (remnant 2) and 227 (remnant 3) revealed shear bands in the vicinity of the impacted surface and near the

mushroomed ends. The W grains in the mushroomed region were transformed from spherical grains to "pancake"-like grains with extremely high aspect ratios. Elongation of W particles also occurred in the shear band regions. Figure 10 is representative of the shear banding observed, and is consistent with the shear banding reported by Lankford, et al. [3-5] for similar alloys. The extremely high aspect ratio of the W grains within the shear bands indicates that the local shear strains exceeded several hundred percent. Matrix fracture and/or melted matrix areas were detected in some of the shear bands investigated and are further evidence of shear instability.

Although shear localization was the predominant form of damage, W particle fracture was observed in some cases on the non-impacted surface (opposite the shear-banded surface) of the remnant. Fracture proceeded through the W particles and appeared to be associated with decohesion of contiguous W particles. Fracture progression through more than three adjacent particles was not detected. The fractured W particles observed at the surface of Shot 227 were concentrated in several regions, and were spaced approximately 30 µm (i.e., a particle spacing) apart. These are illustrated in Fig. 11, taken from the center of the Shot 227 specimen, half-way between two fractured ends (i.e., away from locations where a crack progressed all the way through the rod). These small particle-scale cracks could possibly be examples of widespread initiation sites. However, such fractures are not seen extensively near the fracture surface, and on only one end of the rod are such fractures seen near the actual fracture surface (see Fig. 12). Thus, it is unlikely that many small cracks were uniformly initiated and that the fracture was then dominated by a growth process – i.e., that we should focus on the growth of these small cracks. Rather, understanding initiation is critical.

Optical microscopy evaluations of mounted fracture cross-sections revealed decohesion of adjacent W particles and W particle matrix debonds in the vicinity of "non-mushroomed" fracture surfaces. Fractured W-particles appeared to be associated with these debonds. W-particle fracture was also observed along the fracture path and just beneath the fracture surface as shown in Fig. 13 for Shot 227. The fracture surface features for the reverse ballistic samples are similar to those reported above for the dynamic bend test samples.

Cleavage of W-particles was more apparent upon SEM evaluation of the "non-mushroomed" fracture surfaces. Evidence of intergranular fracture was observed. Dimpled matrix regions were not as prevalent as for the dynamic bend test samples already discussed (*Dynamic Bend* section) for this alloy. Decohesion of W particles from the matrix was detected in isolated locations. Cleavage of numerous W particles was observed parallel to the rod axis. Representative photos of these features are illustrated in Fig. 14. The fracture mode is more brittle than the other test samples evaluated owing to the high loading rate and yawed projectile.

DISCUSSION OF RESULTS AND MODELING

Dynamic fracture of WHA materials is a complex process. Fracture initiated on the surface of the samples provided, and extended into the rod. Both tensile and compressive loading modes were operative. The surface damage was not limited to one location. The failure mechanism involves linkage of isolated, debonded particle-particle regions and debonded particle-matrix regions. Linkage of isolated debonded regions ultimately causes a local reduction in the load carrying capacity of the material in the fracture region. Some plastic flow of the matrix material was observed, but this is dependent on the specific alloy utilized. For example, the W-Ni-Co alloy for the dynamic bend samples exhibited more flow than the W-Ni-Fe alloy in the dynamic transverse fractures based on the extent of matrix dimples observed. Morphology differences were observed across the fracture surfaces. These are attributed to the microstructural damage events rather than strain rate differences across the sample as originally interpreted by Satapathy, et al. [1] for the dynamic bend samples. The metallurgical findings indicate that the fracture process is more complex than continuous propagation of a surface-initiated, brittle crack.

There are two philosophical approaches to modeling fracture. The first is that of the fracture mechanics community, in which a crack is assumed to already be in the material and the question then posed is what is the subsequent behavior of the crack. For a statics problem this question might be, at what load does the crack begin to run? In a dynamical situation, the question might be, given the current transient loads in the body containing a crack, at what speed does the crack extend itself (i.e., at what speed does the crack front propagate)? Usually this school of thought focuses on one crack, or at most a small number of cracks, and then examines the subsequent behavior. The fracture mechanics approach focuses on the stress intensity factor or the transient crack driving force – a measure of the increased stress in the vicinity of the crack tip– to provide information on whether a crack will begin to run or how fast it will propagate. Running cracks then separate material.

The second major school of thought views fracture as beginning with uniformly dispersed small flaws, and then the subsequent loading history on the body gives rise to the growth and coalescence of these flaws. Such an approach is required for understanding spall failure in targets due to high-velocity impacts: the wave interaction gives rise to large tensile regions within the material where voids nucleate and grow, leading to material separation. Examination of a spall surface often reveals very ductile metal behavior, including necking regions where voids have coalesced and allowed the material to separate. The continuum modeling approach to fracture usually assumes an initial flaw distribution and then has stress based growth laws that determine, given the stress state, how fast the voids or microcracks continue to grow. With the void or microcrack distribution known, the material properties are then adjusted to reflect the damage to and reduction in strength of the materials. Material separation occurs when the void density reaches a critical value.

The observations about the tungsten projectiles outlined above indicate two things:

1) An initial fracture begins on the surface and then runs into the projectile. The initial fractures include W-W particle decohesion, W particle-matrix material decohesion, and W particle fracture.

2) Once the crack begins at the surface, a crack runs through the tungsten alloy material. The mechanism may be linkup of W-W particle and/or W particle-matrix decohesion. Large cracks were not seen at the surface; this implies that once a crack reaches a critical size, perhaps on the order of three to four W particles in scale, it leads to catastrophic failure.

Addressing (2) first, the best way to model fracture propagation is with an engineering fracture mechanics approach where the focus is on the pre-existing crack. The crack speed would be determined by examining the stress in the vicinity of the crack and calculating a stress intensity factor or crack driving force. Success with this technique would require some knowledge of the crack velocity versus the crack driving force, but, in the absence of other data, it can be approximated by what is known for other materials (or tests can be performed on the tungsten alloy to determine the relationship – see [7]).

As to the initial crack formation, since it appears that there is not a uniform distribution of flaws along the surface and since large amounts of W particle deformation were not seen in the region of the small cracks (thus implying that use of a criterion based on equivalent plastic strain would not be indicated), the suggested approach would be to assume that a critical tensile stress gave rise to the initial crack formation. Since most isolated small cracks were seen near the surface of the reverse ballistic specimens, an additional requirement would be that fractures initiate on surfaces where there are initial surface flaws. Thus, areas of large tensile stress near the surface are likely initiation points for the fracture. Fractures can be assumed to initiate in such regions, and the calculations can be continued from that point with an assumed initial crack size using the fracture mechanics crack propagation algorithm. Parametric calculations could be performed to see how sensitive the fracture is to the assumed initial crack size.

Unfortunately, most of the current fracture models are not directly helpful for modeling the WHA. They are continuum models and somewhere within them lie assumptions about the growth of the large collection of small cracks or the large collection of voids, both growing the currently existing ones and nucleating new ones. These ideas lie at the heart of Curran and Shockey's NAG/FRAG (for metals) and BFRACT (for geologic materials) [8]. The other approach to a failure model, such as the Johnson-Cook failure model within EPIC, is essentially the response of a metal with a void inclusion, based on the experimental work of Hancock and MacKenzie [9]. They showed that the amount of strain required to initiate failure in the steels

they examined was proportional to the exponential of a constant times the pressure divided by the equivalent (shear) stress:

$$\bar{\varepsilon}^f = \alpha \exp(3p/2\bar{\sigma})$$

Hence, as the pressure increases, the failure strain increases, while for a tensile pressure the failure strain decreases, reflecting the fact that materials are easier to fail in tension. Similarly, little shear means uniform compression or tension, leading to either a large failure strain or a small one, depending on the sign of the pressure. In general, for compression, the larger the shearing stress the smaller the strain required to initiate failure. These ideas and equations have been explicitly incorporated into the Johnson-Cook fracture model so that essentially the damage accumulates at a rate proportional to the stress state as described above. Thus, the model is essentially a void growth model for ductile metals. However, such a model may be useful in predicting the crack initiation location since the damage model includes the effect of stress states, and it is likely that tensile stress is an important component of the crack initiation criteria.

MODELING RECOMMENDATIONS

1) For the near term, the most expedient step is to examine fracture initiation in the tungsten alloy long rods using EPIC. Various fracture criteria could be examined to see which one gives a good prediction for the crack initiation sites along the projectile surface. If the experimental initiation sites are determined by where the rod broke, there is a blurring of the question of initiation and propagation with this approach. To remedy this it may be possible to section the rods to look at the small cracks that did not fully break the rod. The first fracture criterion to examine is simply a maximum tensile stress failure criterion. Impact calculations would be performed with the failure parameter examined throughout the rod for the duration of the impact event to see what critical value or values are reached. The measure of goodness of the failure criterion would be whether it predicts initiation of failure in the regions of known fracture from the experiment, or from small crack sites determined by sectioning the rod.

2) Given that a good initiation criterion has been obtained, the next step is a propagation criterion and modification of EPIC to allow the long-rod projectile to "through-fracture" in the vicinity of fracture initiation. The simplest propagation criterion, and the first tried, would be that the projectile through-fractures once the initiation criterion is reached, and that the crack runs perpendicular to the axis of the projectile. This assumption is valid if the stresses are high enough in the vicinity of the initiated crack tip so that the crack driving force is sufficient to drive the crack through the rod. Modifying EPIC in this fashion will allow the

long-rod projectiles to break during the penetration event. Initiation of a fracture would be based on the initiation criterion from Recommendation (1).

3) After the modification of EPIC and verification of the subroutines, calculations would be performed for detailed comparison with experimental test results. The resulting predicted shapes of the projectile pieces would be compared to the experimentally recovered pieces. This step may reveal limitations of the initiation criterion, and further work may be required to match multiple failure sites. Limitations may become apparent because once the algorithm is in place to allow the rod to break, as upon breaking the subsequent stress state is changed and the location of the next failure may no longer be correctly predicted.

4) If it is felt necessary to perform calculations in CTH (an Eulerian code), CTH will need to be modified to include the failure criterion and rod fracture. This latter topic would be a fairly major effort. One approach might be to have two material numbers defined for the projectile material, and when a crack initiation occurs, change the material on one side of the failure so that they are no longer connected together. This would require a larger effort that the above three recommendations.

5) Finally, it is understood that modeling the fracture process at a basic level is challenging and cannot be adequately addressed using existing fracture models. Since the WHA materials are essentially composite materials consisting of W single crystals in an alloy matrix, modeling of the fracture behavior of these materials at a fundamental level must incorporate the effects of the constituents as they contribute to fracture. Application and extension of composite fracture models available for lower strain rates is suggested as a starting point. Existing models, such as critical strain and brittle fracture, are not directly applicable to the dynamic fracture process of these materials. Strains in excess 100% can occur in shear banded or mushroomed regions of the dynamic fracture samples. Although W particle fracture can occur in these regions, it is clear that the critical strain value varies with microstructure and sample location. The Johnson-Cook void growth EPIC model would require some modification to model the growth matrix voids in a composite material vs. the monolithic material for which it was initially devised. Modeling of the fracture behavior of WHA must involve the effects of the constituents as they contribute to fracture. Since fracture is caused by a series of decohesion events and linkage of these debonded regions, the detailed, fundamental dynamic fracture behavior of WHA is not adequately modeled by the propagation of a single, brittle crack in a monolithic material.

TESTING SUMMARY

1. Metallurgical evaluation of dynamic fracture samples, tested at a range of loading rates, revealed W particle-particle decohesion and W particle-matrix decohesion as the primary forms of damage. The failure mechanism involves linkage of isolated, debonded particle-particle regions and debonded particle-matrix regions. Linkage of isolated debonded regions ultimately causes a local reduction in the load carrying capacity of the material in the fracture region. Decohesion was not as apparent for the reverse ballistic test samples.

2. Fractures of the test samples were surface-initiated, and extended into the rod. The surface damage was not limited to one location and occurred as tensile cracks, W particle fractures and W particle-particle decohesions. Fracture proceeded as a series of isolated events rather than propagation of a single, brittle crack.

3. Some plastic flow of the matrix material was observed in the form of matrix dimples. This is dependent on the specific alloy utilized and the strain rate. The W-Ni-Co dynamic bend test samples exhibited greater dimpling than the W-Ni-Fe dynamic transverse impact samples. Matrix flow was not as apparent for the W-Ni-Co material following reverse ballistic tests.

4. Mushrooming of the impact surface occurred during reverse ballistic testing. This was accompanied by shear localization near mushroomed ends and on surfaces impacted by the target. Shear localization was characterized by shear bands with elongated W grains, and some matrix cracking and localized melting. The extremely high aspect ratio of the W grains within the shear bands is indicative of local shear strain exceeding several hundred percent.

5. The dynamic fracture of WHA is a complex process. Modeling of the fracture process at a fundamental level cannot be adequately addressed using existing fracture models. Since the WHA materials are essentially composite materials consisting of W single crystals in an alloy matrix, modeling of the fracture behavior at a fundamental level must involve the effects of the constituents as they contribute to fracture.

TESTING RECOMMENDATION

1. The samples evaluated in this study were based on several different dynamic fracture tests with a range of strain rates. Improved understanding of the dynamic fracture process of these materials can be obtained by conducting more controlled tests. A dynamic fracture toughness test has been developed recently at SwRI. The test has been utilized to study the dynamics of crack growth in steel at high strain rates 1100 s^{-1}, but can be readily adapted to test other materials. Conducting this dynamic fracture toughness test on WHA samples, in conjunction with fractographic evaluations, will allow monitoring of the fracture process for different crack velocities and energy absorption levels. Direct comparison with low strain rate tests on identical WHA materials will provide better definition of the fracture events. Thus, a more accurate fracture model is possible.

ACKNOWLEDGEMENTS

REFERENCES

1. S. Satapathy, J. Cazamias, S. Bless, R. Gee, L. Meyer and S. Brar, "Dynamic Strength of Tungsten-Nickel-Cobalt Alloys", presented at the 11th APS Topical Group on Shock Compression of Condensed Matter (SCCM), Snowbird, UT, June 27-July 2, 1999.

2. V.Q. Chan, "A New Test Technique to Measure Resistance to Dynamic Fracture of Tungsten Alloys", M.S. Thesis, The University of Texas at Austin, August 1999.

3. J. Lankford, C. E. Anderson, Jr. S. Bodner, "Fracture of Tungsten Heavy Alloys under Impulsive Loading Conditions", J. of Mat. Sci. Ltrs., Vol 7, 1988, p. 1355-1358.

4. J. Lankford, H. Couque, A. Bose, R. German, "Dynamic Deformation and Failure of Tungsten Heavy Alloys", *Tungsten and Tungsten Alloys – Recent Advances*, edited by A. Crowson and E.S. Chen, The Minerals, Metals & Materials, Society, 1991, pp. 151-159.

5. J. Lankford, A. Bose, H.Couque, "High Strain Rate Behavior of Tungsten Heavy Alloys, High Strain Rate Behavior of Refractory Metals and Alloys", edited by R. Asfahani, E. Chen and A. Crowson, The Minerals, Metals & Materials, Society, 1992, pp. 267-287

6. A.Bose, J. Lankford, Jr., and H. Couque, "Dynamic Compressive Properties of Tungsten Heavy Alloys with Varying Grain Sizes" *Processing, Properties and Applications*, Advances in Powder Metallurgy and Particulate Materials, compiled by A. Lawley and A. Swanson, Vol. 4, Metal Powder Industries Federation, Princeton, NJ, 1993.

7. C.E. Anderson, Jr., C.H. Popelar, A. Nagy, and J.D. Walker, "A Novel Method for Determining Dynamic Fracture Toughness," *Shock Compression of Condensed Matter-1999*, edited by M.D. Furnish, L.C. Chhabildas, and R.S. Hixon, American Institute of Physics, Melville, NY, 2000.

8. D.R. Curran, "Dynamic Fracture," Chapter 9 of *Impact Dynamics*, J.A. Zukas, *et al.*, John Wiley and Sons, New York, NY, 1982

9. J.W. Hancock and A.C. MacKenzie, "On the Mechanisms of Ductile Failure in High-Strength Steels Subjected to Multi-Axial Stress-States," Journal of Mechanics and Physics of Solids, Vol. 24, 1976, pp. 147-169.

LIST OF FIGURES

Figure 10 Elongated particles and matrix fracture in a shear band at the impacted surface of Shot 225 following reverse ballistic testing.

Figure 11 Low and high magnification views of W particle fractures on the side surface of Shot 227 following reverse ballistic testing. The surface containing the cracks is located opposite the surface containing the shear-banded regions.

Figure 12 View of one corner of the fracture surface of Shot 227, showing small cracks at the nearby exterior surface.

Figure 13 Enlarged view of the fracture surface of Shot 227 showing particle-particle debonding, particle-matrix debonding and fractured particle.

Figure 14 SEM micrographs of the fracture surface of Shot 227 showing W particle-matrix decohesion, cleaved and faceted W particles.
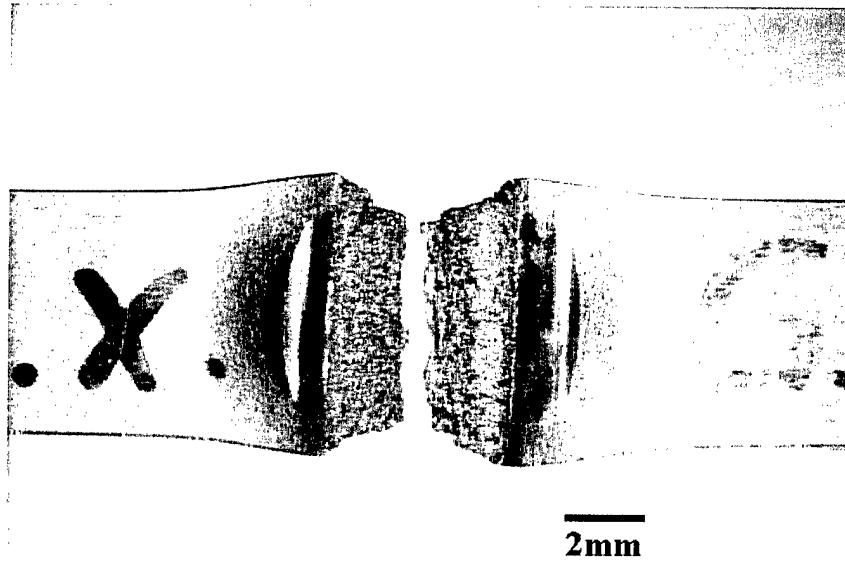
D617
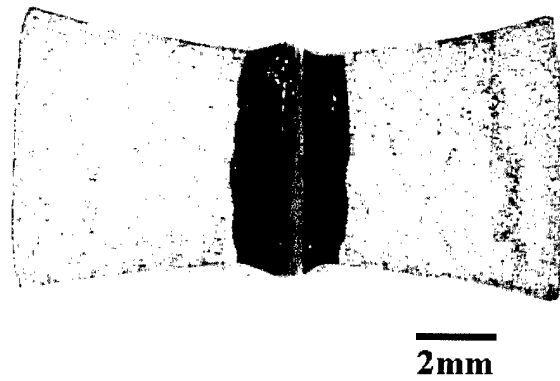
D618

Figure 1. Condition of Sample A following dynamic bend testing. The
bottom photo illustrates the fracture cross-section.

3629
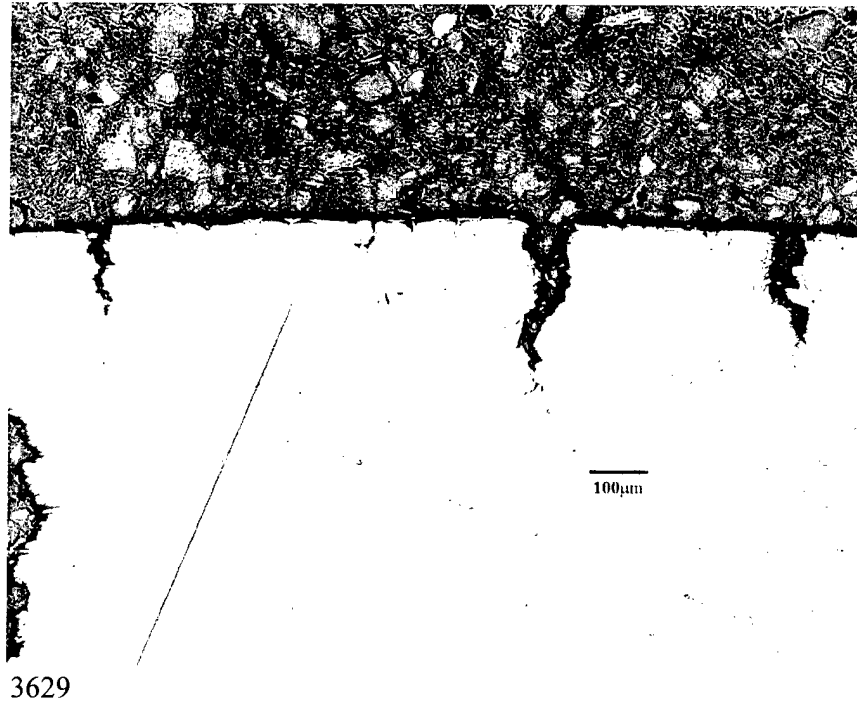
(a) Several tensile cracks in the vicinity of the fracture surface
for Sample A

Figure 2. Tensile cracks on the tensile surface (side opposite the bend surface) of the
dynamic bend test samples.
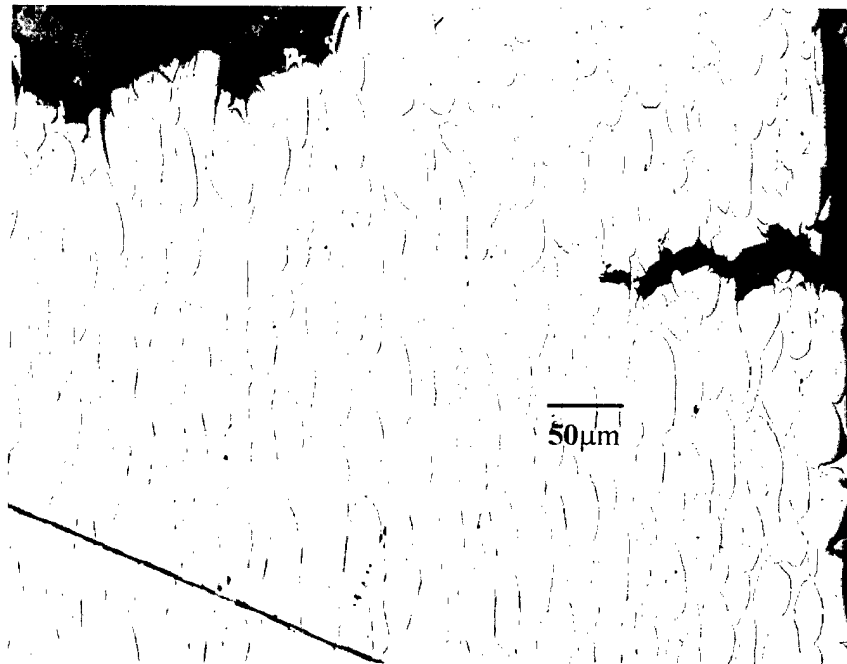
3082

(b)   Enlargement of leftmost crack in (a) for Sample A
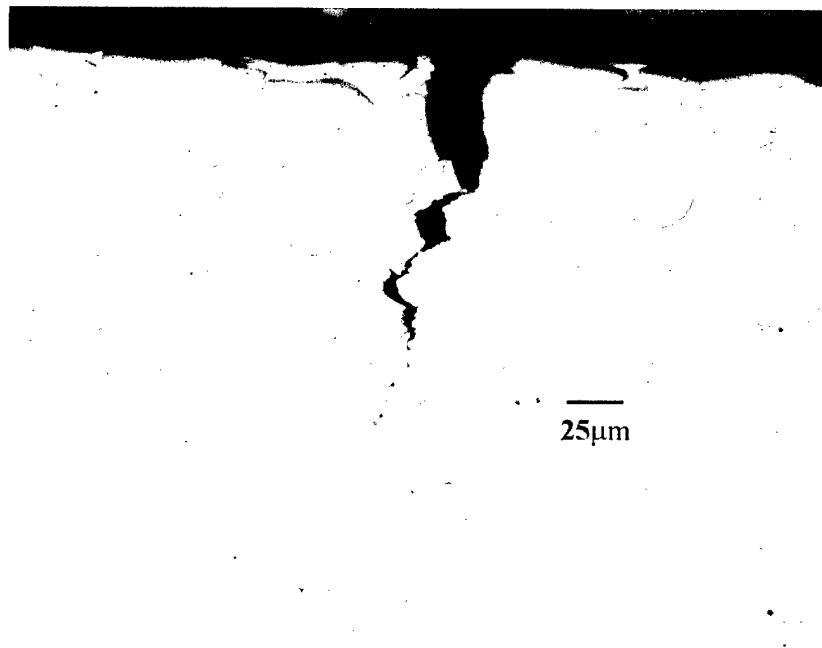
3425

(c)   Enlargement of tensile crack for Sample B showing particle fracture

Figure 2. Tensile cracks on the tensile surface (side opposite the bend surface)
of the dynamic bend test samples (continued).

3084

(a)　Sample A

3631
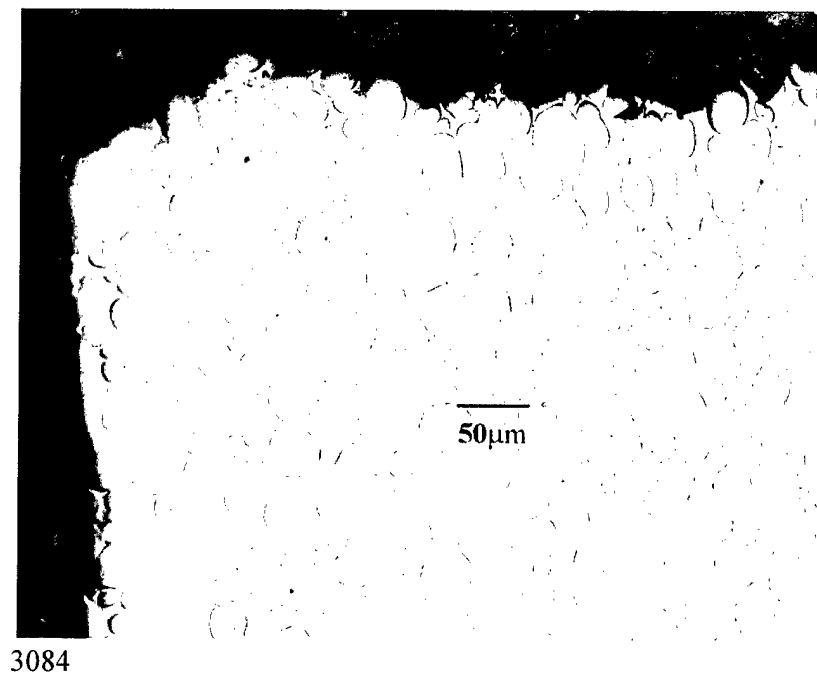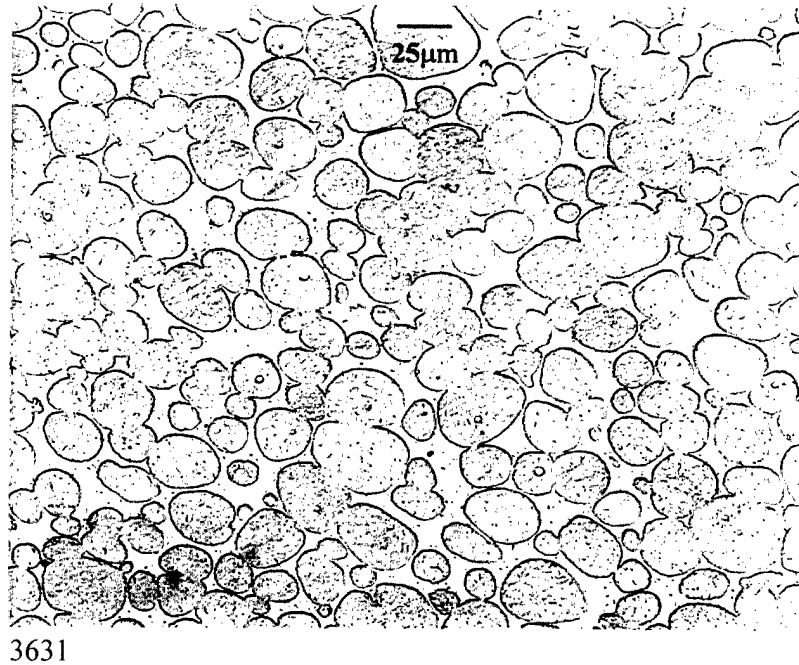
(b)　Sample B

Figure 3. Microstructure on the compressive side of the dynamic bend test samples.

S1134

(a)   Tensile region
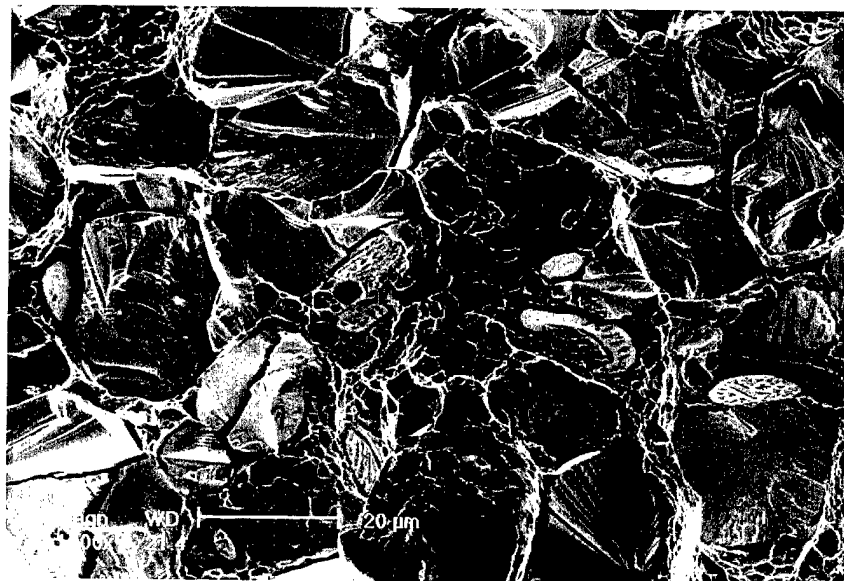
S1137

(b)   Central region of fracture

Figure 4. SEM micrographs of the fracture surface of Dynamic
Bend Sample B.

S1131

(c)   Compressive region
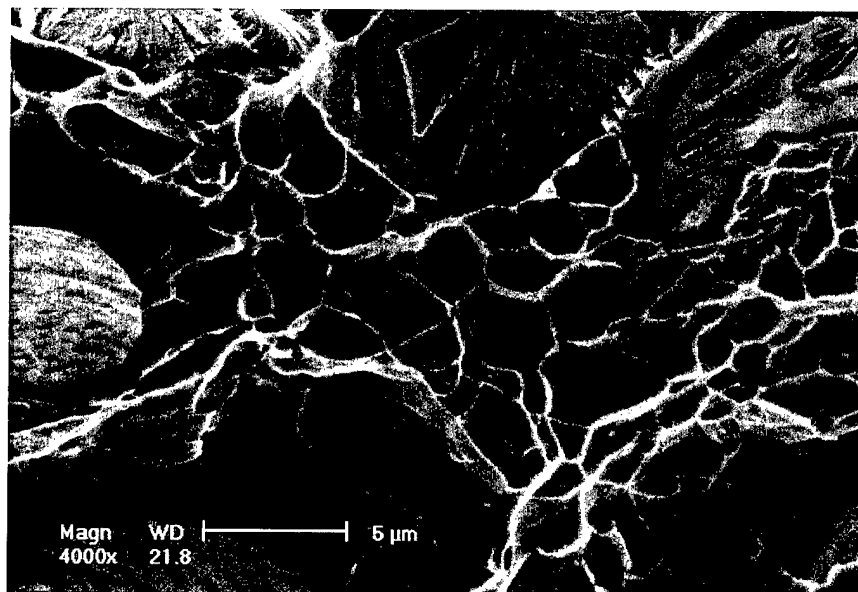
S1130

(d)   Enlargement of (c)

Figure 4. SEM micrographs of the fracture surface of Dynamic

Bend Sample B (continued).
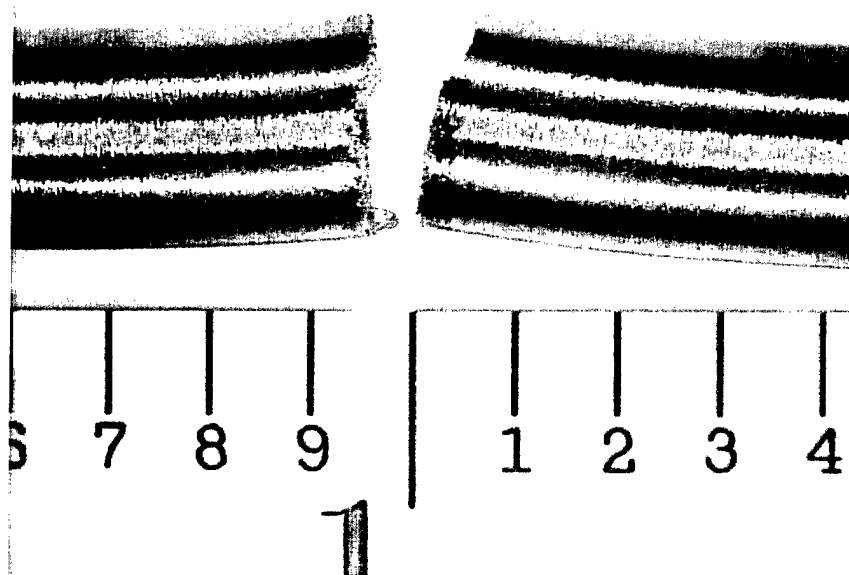
D621

(a)   As-received condition
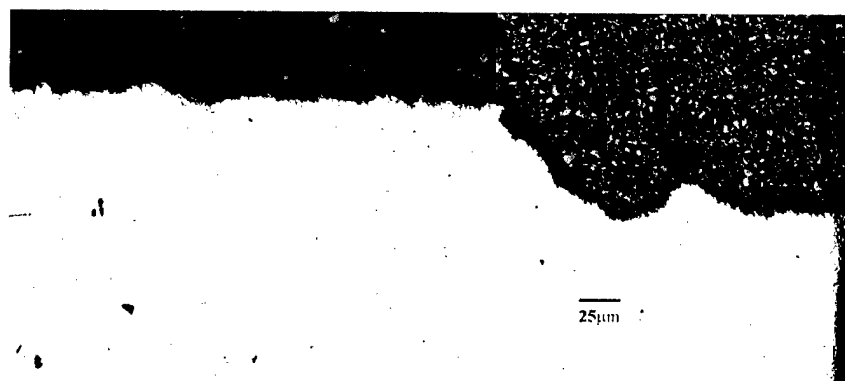
3625, 3626

(b)   Cross-section through the fracture

Figure 5. Fracture of the WHA rod (Shot 74) following dynamic transverse impact
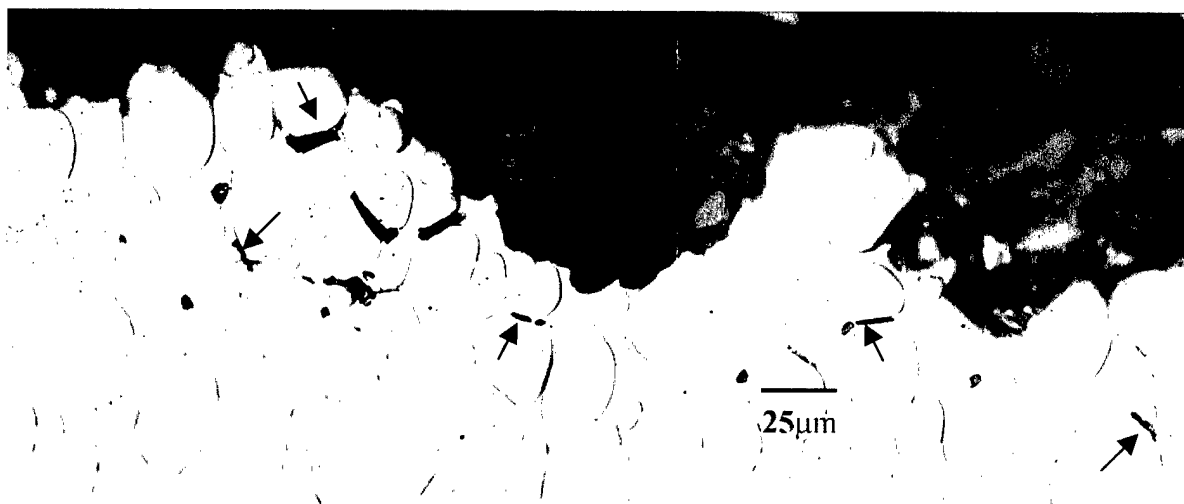
3445, 3444

Figure 6. Optical micrograph of a cross section through the fracture surface of Shot 74. Damage development by decohesion between contiguous tungsten particles and between the tungsten particle-matrix interface is highlighted by the arrows.
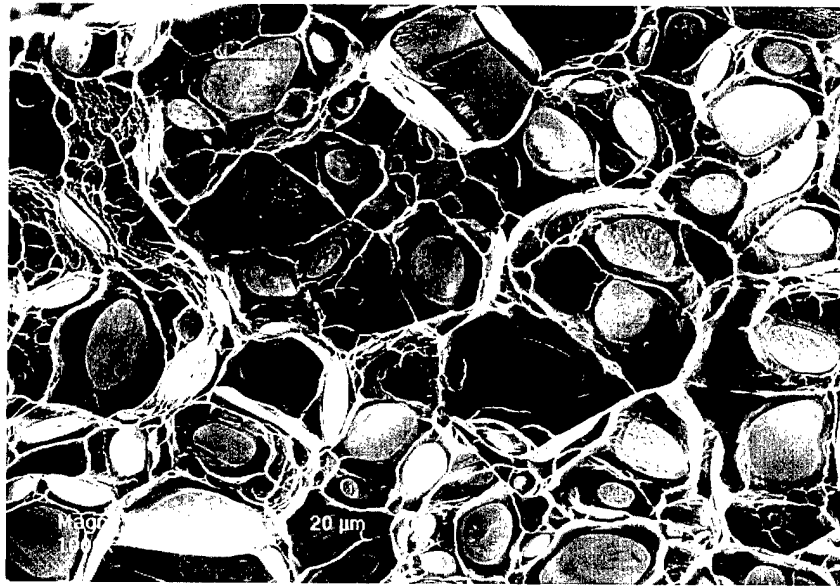
S1155

(a) Tensile region
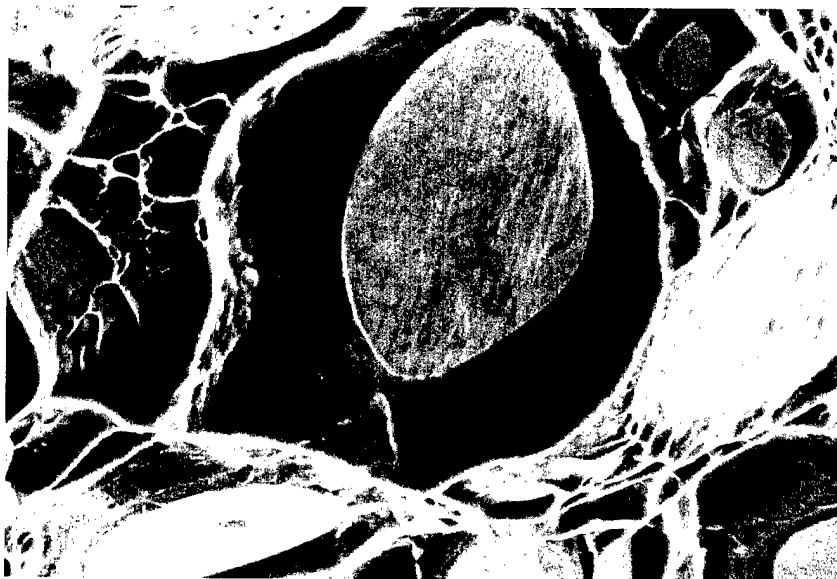
S1156

(b) Enlargement of W facet and matrix decohesion

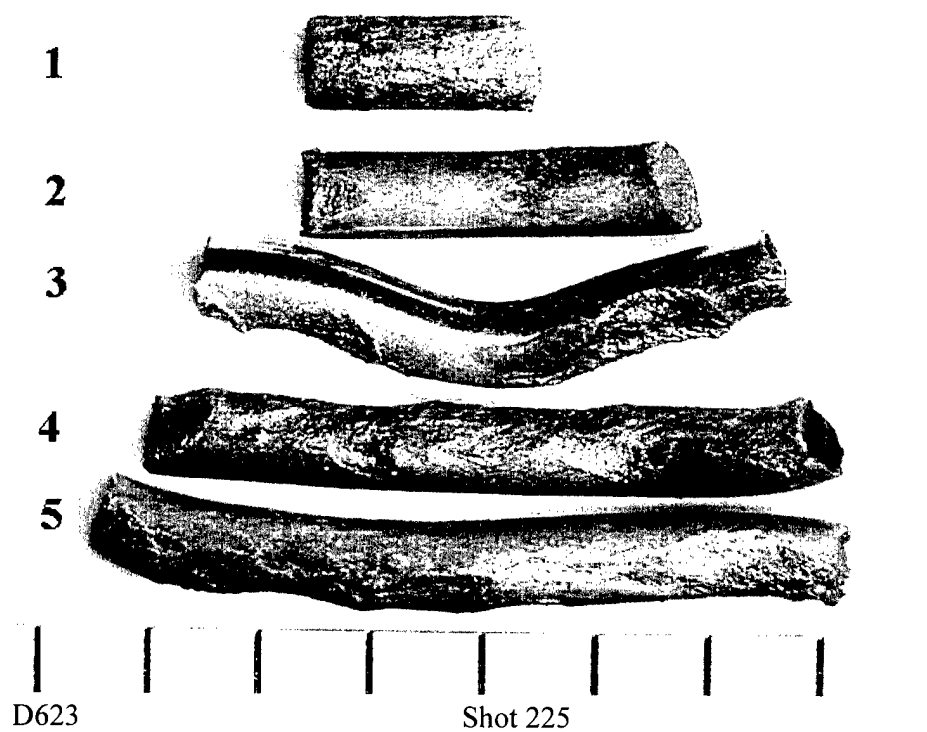Figure 7. SEM micrographs of the fracture surface region of Shot 74, following dynamic transverse impact.
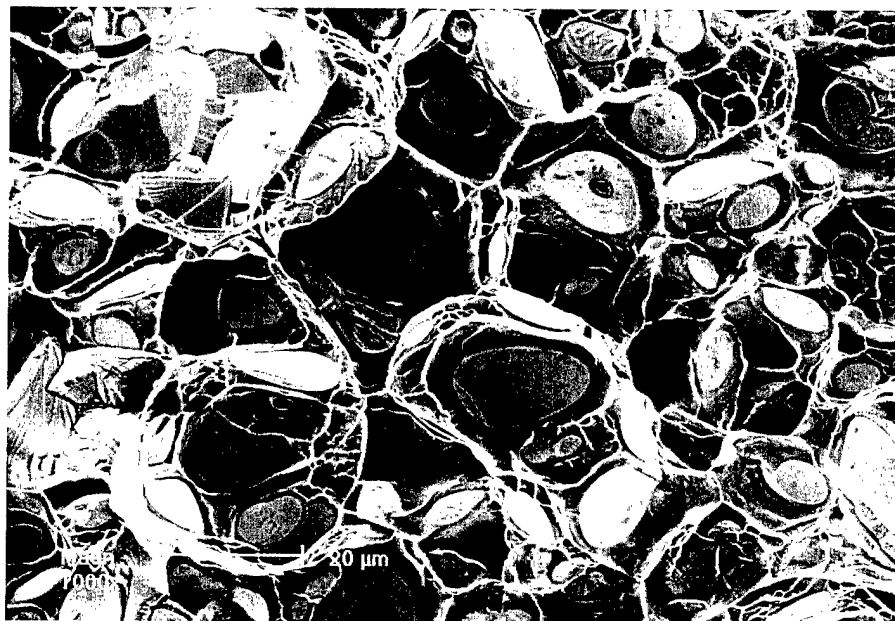
S1157

(c) Central region of fracture
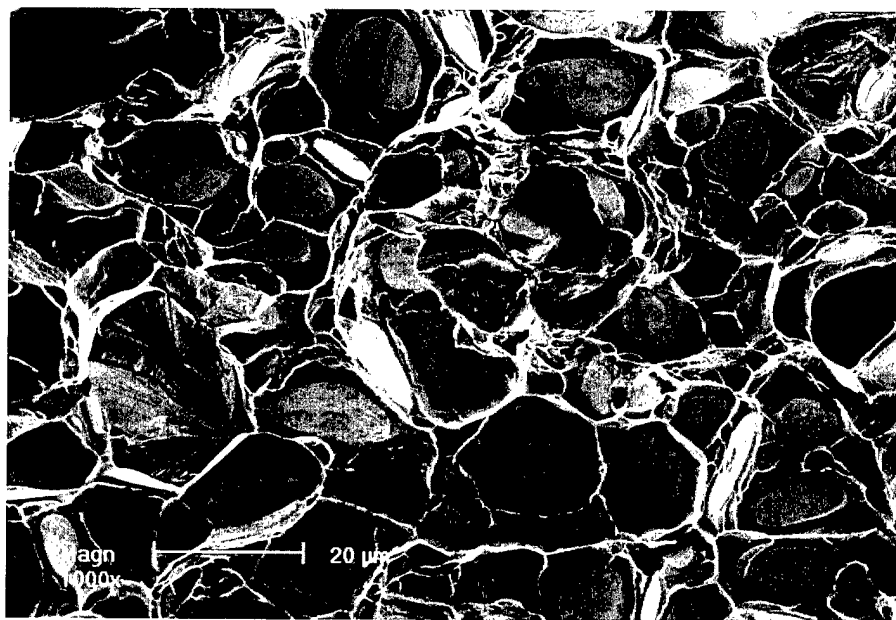
S1162

(d) Compressive region

Figure 7 SEM micrographs of the fracture surface region of Shot 74, following dynamic transverse impact (continued).
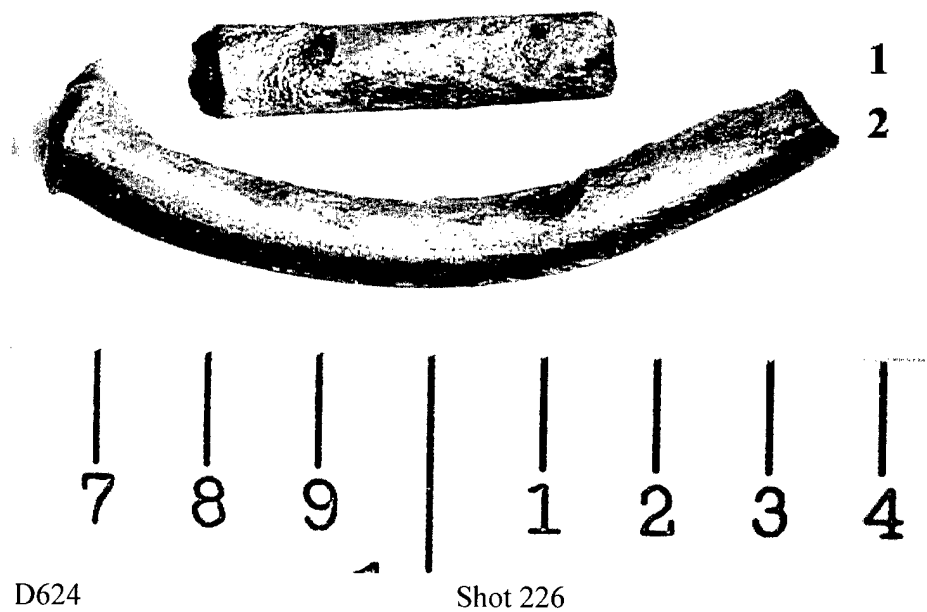
1

2

3

4

5

D623   Shot 225

1
2

7 8 9   1 2 3 4

D624   Shot 226

Figure 8. Overall view of fragments supplied from each of the reverse
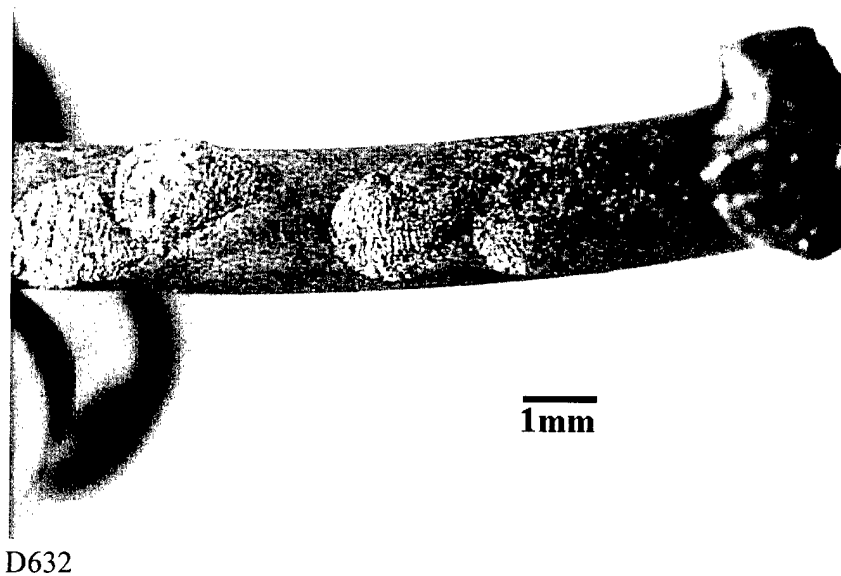   ballistic tests (Shot 225, 226 and 227).

1

2

3

D625   Shot 227
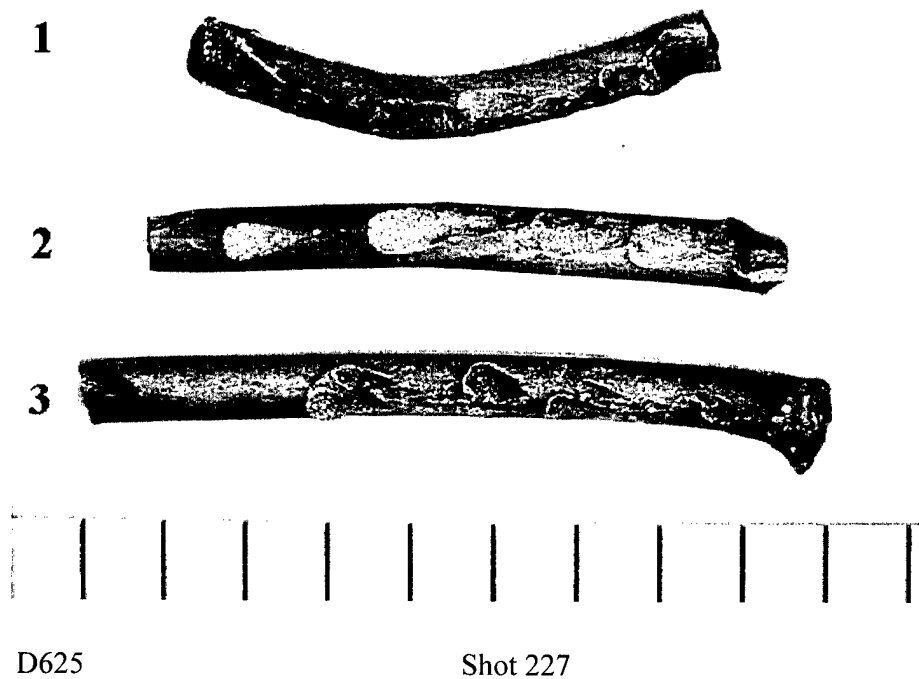
Figure 8. Overall view of fragments supplied from each of the reverse
ballistic tests (Shot 225, 226 and 227) (continued).

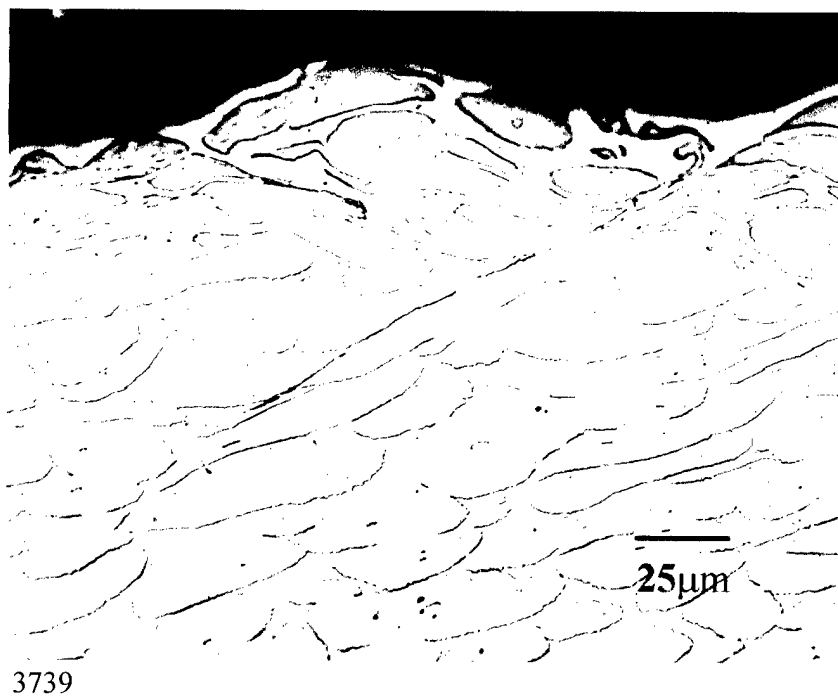Figure 9. Mushroomed fracture surface and impacted regions for Shot 226.

Figure 10. Elongated particles and matrix fracture in a shear band at
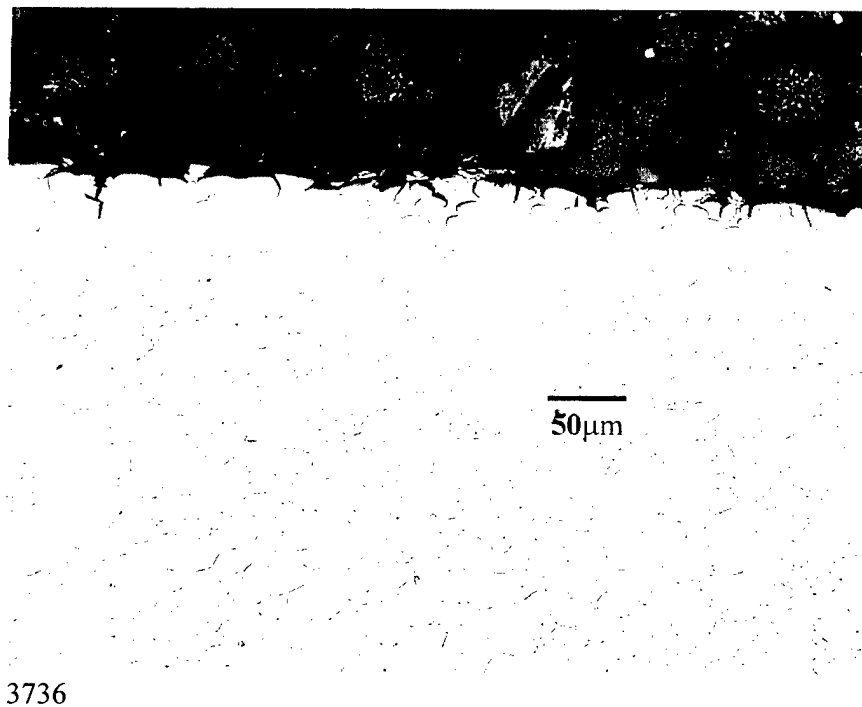the impacted surface of Shot 225 following reverse
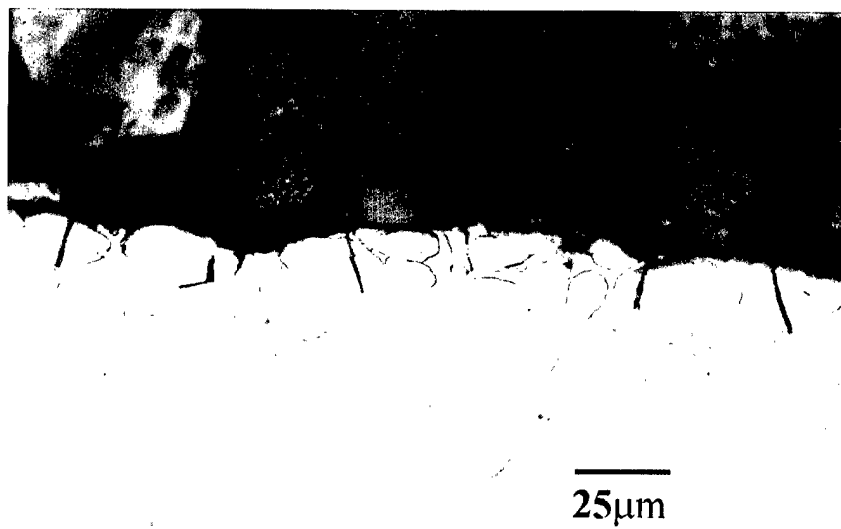ballistic testing.

50μm

3736

Figure 11. Low and high magnification views of W particle fractures on the side surface of Shot 227 following reverse ballistic testing. The surface containing the cracks is located opposite the surface containing the shear-banded regions.

25μm

3737

25μm

3738

Figure 11. Low and high magnification views of W particle fractures on the side surface of Shot 227 following reverse ballistic testing (continued).
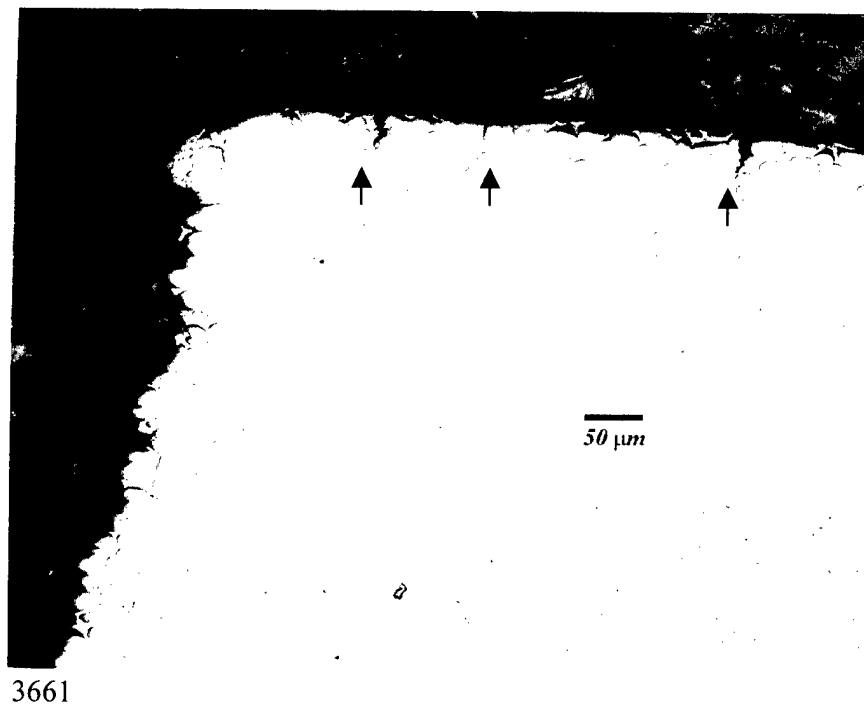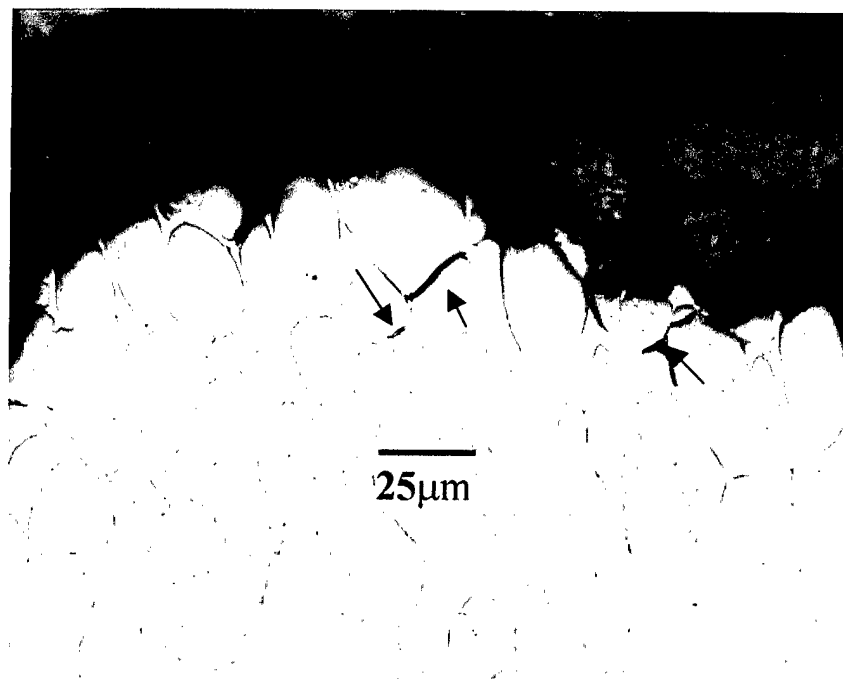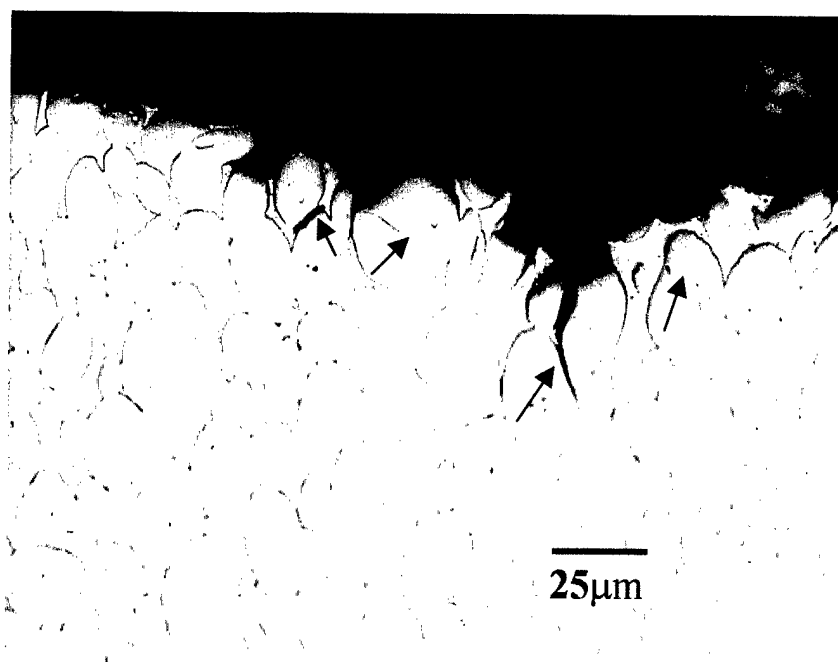
3661

Figure 12. View of one corner of the fracture surface of Shot 227, showing small cracks at the nearby exterior surface.

3743

3741

Figure 13. Enlarged view of the fracture surface of Shot 227 showing particle-particle debonding, particle-matrix debonding and fractured particles.

S1193

(a)

S1189

(b)

Figure 14. SEM micrographs of the fracture surface of Shot 227 showing
W particle-matrix decohesion, cleaved and faceted W particles.

Distribution List

Defense Technical Information Center
Administrator
ATTN: DTIC-DDA
8725 John J. Kingman Road, Suite 944
Ft. Belvoir, VA   22060-6218
USA

Dr. Edward Schmidt
U.S. Army Research Laboratory
ATTN: AMSRL-WM-B
Bldg 4600
Aberdeen Proving Ground, MD   21005-5066
USA

IAT.R 0301